

Photometric determination of the mass accretion rates of pre-main-sequence stars

IX. Recent star formation in the periphery of NGC 346

C. Dik¹ and G. De Marchi²

¹ Leiden Observatory, Leiden University, 2300 RA Leiden, The Netherlands
e-mail: dik@strw.leidenuniv.nl

² European Space Research and Technology Centre, Keplerlaan 1, 2200 AG Noordwijk, The Netherlands
e-mail: gdemarchi@esa.int

Received ; accepted

ABSTRACT

We studied the properties of star formation and the characteristics of young stars in a quiet region located beyond the outskirts of the prominent star-forming cluster NGC 346 in the Small Magellanic Cloud (SMC). Utilising observations from the *Hubble* Space Telescope across the broad *V* and *I* bands, as well as the narrow *H α* band, we identified populations with ages of roughly 10, 60, 400 Myr, and 5 Gyr through isochrone comparison. We successfully identified 137 bona fide pre-main-sequence (PMS) candidates exhibiting *H α* excess with a significance level of 5σ accompanied by an *H α* line emission equivalent width exceeding 20 Å. Physical parameters for these PMS stars were determined, including mass, age, accretion luminosity, and mass accretion rate. Most PMS stars have an age of around 16 Myr and an average mass of $0.80 \pm 0.16 M_{\odot}$. The median mass accretion rate for all 137 PMS stars is estimated to be $\dot{M}_{\text{acc}} \approx 8.0 \times 10^{-9} M_{\odot} \text{yr}^{-1}$. While this rate is lower than that observed in the NGC 346 cluster itself, it is comparable with those measured for PMS stars in low-density star-forming regions in the SMC, despite the absence of apparent clustering and nebulosity. Furthermore, our analysis reveals that the ratios of accreting and non-accreting PMS stars to non-PMS stars and their mass accretion rate correlate with their distance from a group of hot massive stars in the vicinity. This suggests that the ultraviolet radiation emitted by these massive stars might erode the circumstellar discs of nearby PMS stars. Lastly, the overlap between our studied region and observations from the *James Webb* Space Telescope reveals that some of the identified PMS stars display near-IR excess.

Key words. stars: formation – stars: pre-main sequence – Magellanic Clouds – galaxies: star clusters: individual: NGC 346

1. Introduction

The process of star formation is a complex and fundamental phenomenon in astrophysics, and is intricately connected to the evolution of galaxies and star systems. It begins with the collapse of gas clouds; this leads to the formation of protostars, which eventually evolve into stable main sequence (MS) stars — the predominant stage of a star's life, including our own Sun (McKee & Ostriker 2007). Models of star formation have been refined over time, incorporating various physical factors such as turbulence (Shu et al. 1987), magnetic fields (Crutcher 1999), and radiation (Krumholz et al. 2012).

The environment plays a critical role in shaping the process of star formation. Factors such as gas density, temperature, and metallicity exert significant influence on the fragmentation and subsequent properties of forming stars (Nozaki & Machida 2023). High-density environments tend to favour the formation of more massive stars, while the presence of young massive stars can either stimulate or hinder the star formation process through their winds and radiation (Haid et al. 2018). Similarly, variations in metallicity are known to affect the rates of mass accretion, thereby influencing the evolution of star-forming regions (De Marchi et al. 2017, 2024). The conditions of low-metallicity regions are more comparable to those of the early Universe and thereby provide useful information on the star formation process in the past (see e.g. Madden et al. 2013; Bromm 2013).

Furthermore, studying star formation outside the boundaries of a massive cluster offers a unique opportunity to test how far the influence of clustered, high-mass star formation extends into the surrounding lower-density field.

In this work we probe the conditions mentioned above by studying a field in the periphery of the NGC 346 starburst cluster in the Small Magellanic Cloud (SMC). This field has a low metallicity, a low density, and is close to a massive cluster, conditions thought to be common in the early Universe. Such environments are known to respond differently to radiative and mechanical feedback compared to more metal-rich, higher-density star-forming regions (see e.g. Krumholz 2012; Rémy-Ruyer et al. 2014). We searched for, identified, and characterised accreting pre-main-sequence (PMS) stars, investigated their physical properties, and assessed how the local environment shapes the star formation process in this diffuse region.

The structure of the paper is as follows: In Section 2 we present the data and observations. Section 3 describes the photometric analysis of the data, including the colour-magnitude diagram (CMD) and the necessary corrections. In Section 4 we discuss how to identify PMS stars and present the properties of the PMS population in the studied region. In Section 5 we derive the effect of nearby stars on star formation. Section 6 contains a comparison with recent *James Webb* Space Telescope (JWST)

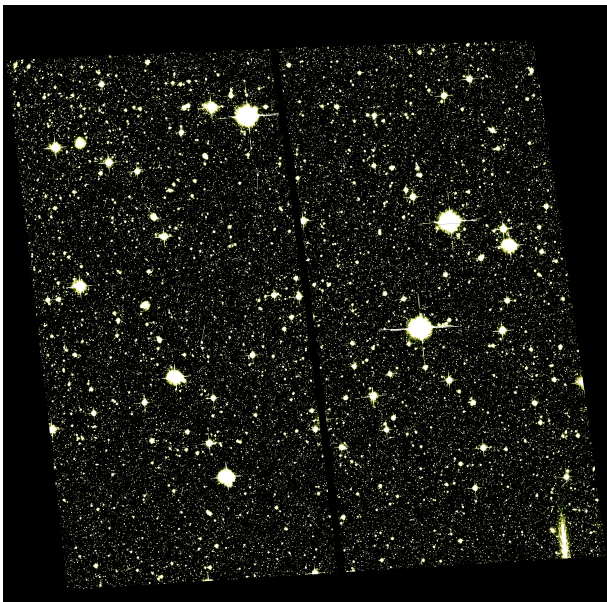


Fig. 1. Colour image of the studied field south of NGC346, created by combining the HST *V*- and *I*-band images.

observations in the region. Finally, a summary and conclusions are provided in Section 7.

2. Observations

This work mainly uses observations collected with the *Hubble* Space Telescope (HST), in the F555W band (hereafter ‘*V* band’), F814W band (‘*I* band’), and F656N band (‘*H α* band’), with exposure times of 1200 s, 400 s and 2394 s, respectively. The observations in the *V* and *I* band were executed with the Wide Field Channel on the Advanced Camera for Surveys (WFC/ACS) in July 2004 under the HST proposal ID 10248 (A. Nota). The narrow-band *H α* images were obtained with the Ultraviolet/Visible channel of the Wide Field Camera 3 (UVIS/WFC3), in August 2013 under the HST proposal ID 13009 (G. De Marchi). Both proposals have the goal of studying star formation in the SMC and characterising PMS stars (Nota et al. 2006). The *H α* images covered regions with preexisting *V* and *I* observations, in order to identify PMS stars, and derive accretion luminosities and mass accretion rates of the studied objects directly from the photometry (De Marchi et al. 2011a). The studied region can be seen in colour in Fig. 1. The field spans $200'' \times 200''$, corresponding to $\sim 60 \times 60$ pc at a distance of 62.5 kpc (Graczyk et al. 2020), and lies to the south of the main cluster NGC 346.

In addition to the HST images, this work uses JWST photometry of a nearby field to make comparisons with the studied region. This consists of observations using the NIRCcam instrument in the F090W, F115W, F182M, F187N, F277W, F356W, F405N, and F430M filters. These observations were carried out as part of programme 1227 (M. Meixner) in July 2022. The objective of the programme is a comprehensive imaging and spectroscopic study of the cluster NGC 346 (Jones et al. 2023; De Marchi et al. 2024). During the spectroscopic observations of the cluster with NIRSpc, NIRCcam was used to observe in parallel a field located about $10'$ south of the cluster. The area covered in this way spans from the cluster edge southwards towards the field studied with HST. There is a small corner of the NIRCcam field of view (B side of the camera) that overlaps with the *V*, *I*, and *H α* images (top left in Fig. 1). The relative positions of the

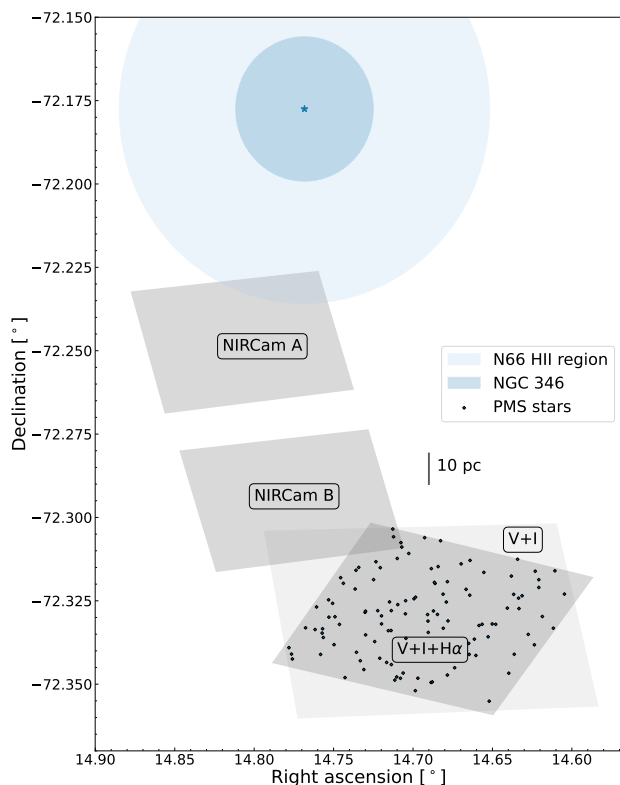


Fig. 2. Regions observed with HST and JWST, and the rough extent of the cluster NGC 346 and the surrounding HII region N66.

HST and JWST fields — including the overlapping region — as well as the approximate extent of the NGC 346 cluster can be seen in Fig. 2. Table 1 lists the observations used in this work.

Table 1. List of observations.

Camera	Filter	Time [s]	RA	Dec
WFC/ACS	F555W	1200	14.6880	-72.3307
WFC/ACS	F814W	400	14.6880	-72.3307
UVIS/WFC3	F656N	2394	14.6880	-72.3307
NIRCcam	F090W	299	14.7917	-72.2711
NIRCcam	F115W	299	14.7917	-72.2711
NIRCcam	F182M	299	14.7917	-72.2711
NIRCcam	F187N	1353	14.7917	-72.2711
NIRCcam	F277W	299	14.7917	-72.2711
NIRCcam	F356W	299	14.7917	-72.2711
NIRCcam	F405N	1353	14.7917	-72.2711
NIRCcam	F430M	299	14.7917	-72.2711

Notes. The observations obtained with the HST are listed in the top panel, those with JWST at the bottom. Exposure times are in second, right ascension (RA) and declination (Dec) in decimal degree.

3. Photometric analysis

The *V*, *I*, and *H α* images were retrieved from the HST archive and had already been processed through the standard calibration

pipelines for the ACS (V and I bands) and WFC3 ($H\alpha$ band) instruments, which account for bias subtraction, flat-fielding, dark correction, and image drizzling. We used the DAOPHOT routine in IRAF on all images to perform the source detection and photometry, running the detection step on the I -band image because it is the deepest. Sources were selected using an aperture radius of 2 pixels, and we required their peak flux to exceed the local background by at least 5σ . The background was measured in an annulus between 3 and 5 pixels from the source centre, with σ defined as the standard deviation of the counts within this annulus. Photometric uncertainties were computed with the DAOPHOT routine from photon-noise statistics of the source and from the background variance within the aperture, and were propagated into magnitude uncertainties using standard error-propagation formulas. This procedure yielded 42 299 sources in the I -band image, of which 42 168 have counterparts detected in the V band.

The $H\alpha$ observations were taken with a different camera and were therefore registered with the V - and I -band images to have the same World Coordinate System astrometry. For this we used as a reference a bright, unsaturated source visible in all images.

Since the telescope point spread function extends beyond our adopted aperture radius of 2 pixels, it is necessary to correct the measured stellar fluxes for the fraction of the total energy that falls outside this aperture. Following the encircled-energy curves for the ACS/WFC instrument derived by Bohlin (2016), we computed an aperture-correction factor equal to the encircled-energy fraction at 2 pixels, minus the difference between the fractions at 5 and 3 pixels. This subtraction accounts for the flux contained in the background annulus (3–5 pixels) used in our photometric routine. The resulting factor was applied to all instrumental fluxes to recover the total source flux. As for the photometric zero points, these were taken from the ACS Zeropoint Calculator¹ and from Kalirai et al. (2009) for the WFC3 $H\alpha$ filter, and were used to convert the aperture-corrected fluxes into calibrated magnitudes according to the standard HST VEGAMag photometric system. These values are listed in Table 2.

Table 2. Encircled energies and zero-point magnitudes for the different bands.

Band	Encircled energy fraction	Zero-point magnitude
I	0.528	25.520
V	0.594	25.733
$H\alpha$	0.469	19.920

We limited our study to the 25482 sources with a combined uncertainty in the V and I bands $\sigma_{VI} \leq 0.1$. Considering the uncertainties in the $H\alpha$ image, which is noisier due to the narrow-band filter, we required $\sigma_{H\alpha} \leq 0.3$ in addition to our σ_{VI} uncertainty selection. This further constraint limits to 12649 the total number of sources that we consider to have solid photometry. Table 3 lists the position, magnitude, and uncertainty for the first few sources. The full table is available online.

With the exposure times used in the V and I bands (see Table 1), the brightest objects in the field are saturated or affected by photometric non-linearity. To be conservative, we considered all stars brighter than $V = 19$ mag to be affected by lack of linearity or saturation and retrieved their magnitudes using *Gaia*. For each of these sources, we visually matched it to the corresponding object in the *Gaia* Data Release 3 (DR3) catalogue (Gaia Collaboration et al. 2023) and retrieved the respective

G , G_{BP} and G_{RP} magnitudes. These were converted to V and I magnitudes using known photometric conversions². Of the original 167 sources with $V < 19$ mag, 100 have their magnitudes retrieved from the *Gaia* catalogue.

The resulting CMD is shown in Fig. 3. Clearly visible is the MS, as well as a red-giants red clump around $V \approx 19$ mag and $(V - I) \approx 1.0$ mag, with the majority of stars populating the bottom of the MS. The objects with magnitudes retrieved from *Gaia* are indicated as orange dots in Fig. 3.

Also shown in the CMD are isochrones obtained from Bressan et al. (2012), Pastorelli et al. (2019), Tang et al. (2014), and Chen et al. (2019), for the specific HST ACS/WFC photometric system (Girardi et al. 2008) and metallicity $Z = 0.004$. The isochrones correspond to ages of 10, 60, 400 Myr, and 5 Gyr. Although the slightly elongated shape of the red clump suggests that some differential reddening might be present in the field (see e.g. De Marchi & Panagia 2014), its effects are small and for the reddening correction we only consider the component due to the Galactic foreground, corresponding to $E(V - I) = 0.16$ mag, following the approach of Sabbi et al. (2007), with a spread of about 0.04 mag (Hennekemper et al. 2008). Indeed, after correcting the isochrones for this foreground extinction, they follow the observations closely. We see that the brightest stars reach $V \approx 15$ mag and closely follow the 10 Myr isochrone, corresponding to a young population of recently formed massive stars. At $V \approx 16$ mag, we see signs of a population of roughly 60 Myr old red supergiants. Further down, there is a clear horizontal group, which we associate with an old population of around 400 Myr old. Finally, the oldest stars in the field correspond to an age of several gigayears.

4. Pre-main-sequence stars

Using our photometric catalogue, we searched for PMS candidates by identifying stars with significant $H\alpha$ emission.

Pre-main-sequence candidates were identified through their $H\alpha$ excess in the $(V - H\alpha)$ versus $(V - I)$ colour-colour diagram (Fig. 4). In particular, we searched for sources whose $V - H\alpha$ colour exceeds that of ‘normal’ (i.e. MS) stars with the same $V - I$ by at least $5\sigma_{VH\alpha}$ or 5 times the combined photometric uncertainty in V and $H\alpha$ (hereafter 5σ excess). We used model atmospheres by Bessell et al. (1998) for the specific metallicity of the SMC ($1/8 < Z/Z_{\odot} < 1/5$; Russell & Dopita 1992; Rolleston et al. 1999) to determine the expected $V - H\alpha$ colour of MS stars (dashed line in Fig. 4). Stars whose observed $V - H\alpha$ colour exceeds the photospheric value by at least 5σ were flagged as $H\alpha$ -excess sources (orange dots in Fig. 4).

We then estimated the $H\alpha$ equivalent width $W_{eq}(H\alpha)$ from the observed $H\alpha$ magnitude, following the photometric method discussed in De Marchi et al. (2010). This allows us to quantify the strength of the emission line even without spectroscopy. Besides requiring that objects have $H\alpha$ excess $> 5\sigma$, we also imposed the condition that the $H\alpha$ emission equivalent width must be at least 20 \AA in absolute terms, in order to exclude low-mass stars possibly affected by chromospheric activity (see e.g. White & Basri 2003). Finally, we imposed a photometric quality criterion requiring that the combined uncertainty,

$$\delta_3 = \sqrt{\frac{\sigma_V^2 + \sigma_I^2 + \sigma_{H\alpha}^2}{3}},$$

² https://gea.esac.esa.int/archive/documentation/GEDR3/Data_processing/chap_cu5pho/cu5pho_sec_photSystem/cu5pho_ssec_photRelations.html#Ch5.T7

¹ <https://acszeropoints.stsci.edu/>

Table 3. Photometric catalogue for the 12649 sources with good photometry (extract).

ID	RA	Dec	V	δV	I	δI	$H\alpha$	$\delta H\alpha$
1	14.661975	-72.357890	27.62	0.08	23.97	0.03	24.42	0.23
2	14.659048	-72.357840	25.35	0.03	19.88	0.01	20.77	0.04
3	14.662388	-72.357700	23.49	0.01	22.64	0.02	22.29	0.09
4	14.657059	-72.357651	23.49	0.01	22.62	0.02	23.13	0.13
5	14.652981	-72.357649	24.73	0.02	23.70	0.03	23.28	0.14
6	14.660612	-72.357628	24.40	0.02	23.47	0.03	24.24	0.21
7	14.651501	-72.357611	23.32	0.01	22.42	0.02	22.94	0.12
8	14.664865	-72.357595	23.93	0.01	23.01	0.02	22.62	0.10
9	14.662593	-72.357611	24.72	0.02	23.67	0.03	23.93	0.18
10	14.652131	-72.357592	23.44	0.01	22.58	0.02	22.83	0.11

Notes. For each source, the table lists the identification number (ID), the coordinates (RA and Dec in decimal degree), and the magnitudes in the V , I , and $H\alpha$ bands, together with their uncertainties. Only the first ten lines are shown here; the complete catalogue is available in electronic form at the CDS.

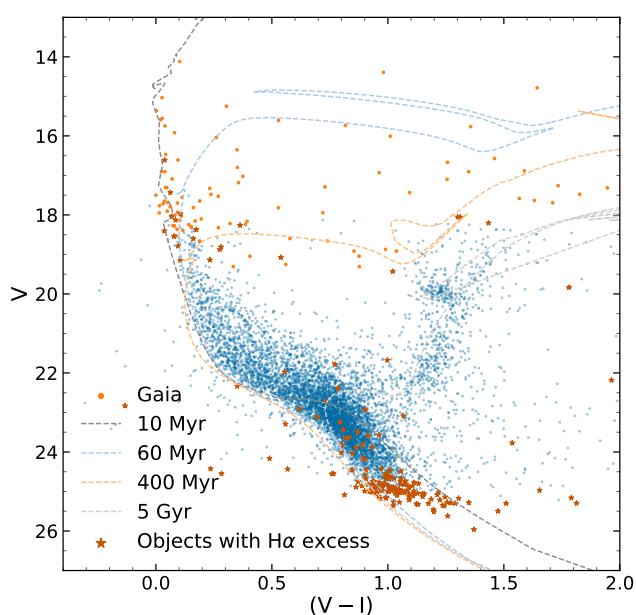


Fig. 3. CMD showing the V magnitude as a function of the $V - I$ colour of the stars in the studied region. Shown in orange are the (potentially) saturated stars that were recovered through *Gaia*. In brown are the objects with $H\alpha$ excess emission as identified in Section 4. The dashed lines represent isochrones for 10 Myr, 60 Myr, 400 Myr, and 5 Gyr.

be ≤ 0.08 mag, as in De Marchi et al. (2010), where σ_V , σ_I , and $\sigma_{H\alpha}$ are the photometric uncertainties in the three bands. Only stars meeting all three conditions ($\geq 5\sigma_{VH\alpha}$ excess, $|W_{eq}(H\alpha)| \geq 20 \text{ \AA}$, and $\delta_3 \leq 0.08$ mag) were retained as robust PMS candidates with significant $H\alpha$ emission.

Of the 12649 objects with solid photometry selected above, 7302 sources satisfy this combined uncertainty constraint, and are plotted in dark grey in Fig. 4. Out of this sample, a total of 192 sources have both a 5σ significant $H\alpha$ excess and $|W_{eq}(H\alpha)| \geq 20 \text{ \AA}$ in emission, and can therefore be identified as bona fide PMS stars.

We note that the sample might still include Be stars, which usually exceed the set equivalent width threshold as a result of strong stellar winds (see e.g. McSwain & Gies 2005). As we

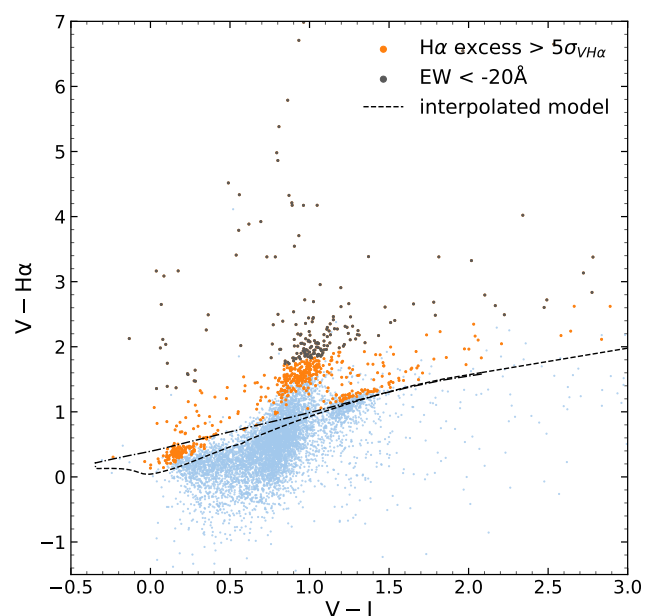


Fig. 4. Colour-colour diagram of the sources in the studied region with $\delta_3 \leq 0.08$ mag. The dashed line indicates the curve interpolated from the model atmospheres by Bessell et al. (1998), whereas the dot-dashed line indicates the continuum. In orange are the objects with $H\alpha$ excess greater than 5 times the uncertainty on $V - H\alpha$. The dark grey points are the sources that exhibit an emission equivalent $|W_{eq}(H\alpha)| \geq 20 \text{ \AA}$.

discuss in the next section, these stars will be excluded and our selection will be further narrowed down when we determine the physical properties of the candidate PMS objects.

The PMS candidates are shown in brown in the CMD in Fig. 3. The majority of sources are fainter than $V \simeq 24$ mag and there are objects both on the ‘red side’ of the MS, where younger objects are expected, and closer to the MS itself, where more evolved PMS stars should be. At the top of the distribution, at magnitudes $V \lesssim 19.5$, we have another group of sources, which likely contain the aforementioned Be stars.

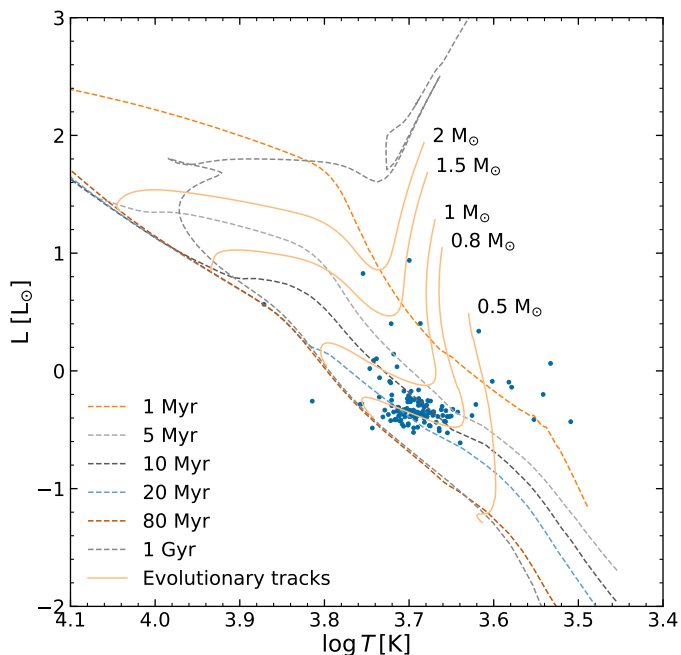


Fig. 5. HR diagram of the PMS candidates in the studied region. Shown are the isochrones and evolutionary tracks from Tognelli et al. (2011). The blue points indicate bona fide PMS stars.

4.1. Properties of PMS stars

Following De Marchi et al. (2010), the effective temperature (T_{eff}) was obtained by interpolating the model atmospheres by Bessell et al. (1998) in the specific HST bands of our study, as a function of the $V - I$ colour. Using the same model atmospheres, we determined the radius of the star in solar units as

$$R = \sqrt{10^{-0.4(M_V - M_{V,\text{ref}})}}, \quad (1)$$

where M_V is the absolute V magnitude, calculated using a distance modulus of 18.98 from the distance to the SMC of 62.4 kpc (Graczyk et al. 2020). $M_{V,\text{ref}}$ is the absolute V magnitude derived from the theoretical Bessell et al. (1998) model atmospheres for a $1 R_{\odot}$ star. With the radii and effective temperatures of the stars, the bolometric luminosities (L_{bol}) were derived, in solar units, from the Stefan–Boltzmann law, using a solar effective temperature $T_{\odot} = 5778$ K (Cox 2000). The typical uncertainty on T_{eff} is of the order of 150 K, while that on L_{bol} is approximately 5%.

From the derived L_{bol} and T_{eff} , we constructed a Hertzsprung–Russell (HR) diagram, as shown in Fig. 5. As a reference, the evolutionary tracks of Tognelli et al. (2011) are added for masses in the range $0.5 - 2.0 M_{\odot}$, ages younger than 100 Myr, and metallicity $Z = 0.004$, as appropriate for the SMC. We only include in this diagram the location of the 137 bona fide PMS stars, to which the evolutionary tracks apply. Only for these stars can a reliable mass and age be obtained (for the same reason, we have also excluded likely Be stars).

Stellar masses and ages of the bona fide PMS candidates were derived using a probabilistic comparison with evolutionary tracks, following the ‘sieve’ method outlined by Romaniello (1998) and later refined by De Marchi et al. (2011a, 2011b, 2013, 2017). The PMS evolutionary tracks are first resampled to build a fine grid in the HR diagram, interpolated between major evolutionary phases. For each star, the observational uncertainties in T_{eff} and L_{bol} define a cell in the HR diagram. All evolutionary tracks crossing this cell contribute possible age–mass solutions,

weighted by the evolutionary time spent in the cell. The resulting probability distributions yield the most likely mass and age and their associated uncertainties. The procedure is discussed by De Marchi et al. (2017), to whom we refer the reader for further details. In the end, we were able to derive physical parameters for all 137 PMS stars and to measure the associated statistical uncertainties.

While the positions of PMS stars in the HR diagram allow us to estimate their masses and ages, it is well known that individual PMS ages derived from isochrone comparison can be highly uncertain, owing to the tight spacing of isochrones at early evolutionary stages (see e.g. Baraffe et al. 2002; Hillenbrand & White 2004; Bell et al. 2013; Jeffries et al. 2017). Masses are generally more robust, since evolutionary tracks of different masses remain well separated over the relevant temperature range. In the low-metallicity environment of the Magellanic Clouds, however, PMS stars evolve more rapidly across the HR diagram, and the isochrones are correspondingly more widely spaced, reducing the relative age uncertainty by more than a factor of 2 compared to solar metallicity regions (De Marchi et al. 2024).

The distribution of derived ages and masses is shown in the top panels of Fig. 6. The uncertainties on $\log T_{\text{eff}}$ and $\log L_{\text{bol}}$ primarily come from the photometry and are roughly constant across the CMD (and HR diagram), but as the age increases, the separation between isochrones becomes progressively smaller. A typical $V - I$ difference of 0.1 mag between the colours of two PMS stars in the CMD could imply an age difference of ~ 2 Myr at ages around 4 Myr, growing to a difference of ~ 7 Myr around an age of 20 Myr. For this reason, in Fig. 6 we adopted for the ages a logarithmic step of $\sqrt{2}$, which is always wider than the observational uncertainties (see De Marchi et al. 2011b). We used the median age of 16 Myr to split the population in a ‘young’ and an ‘old’ group, containing respectively 63 stars (shown in orange in Fig. 6) and 74 stars (blue).

Considering the masses of the PMS stars, there is a difference between the young and old populations. The top-right panel of Fig. 6 shows the PMS mass distribution. Most stars are subsolar in mass, around $0.7 - 0.9 M_{\odot}$. The mass distribution of old PMS stars is sharply peaked with a mean of $0.77 M_{\odot}$ and a standard deviation of $0.05 M_{\odot}$. The young PMS population has two peaks, with a small group of stars at $0.45 M_{\odot}$ and a much more numerous and broader distribution peaked at $0.85 M_{\odot}$ with a standard deviation of $0.22 M_{\odot}$. The median mass values are also shown in the figure (vertical dashed lines).

The observed pattern is not unexpected. At the earliest stages of star formation, stars of all masses are still in the PMS phase and typically show active accretion, and hence significant $H\alpha$ excess. As time goes by, however, accretion progressively weakens, and this decline occurs more rapidly in the more massive PMS stars, which contract and reach the MS on shorter timescales. As a consequence, at later evolutionary stages the sources that still satisfy our strict $|W_{\text{eq}}(H\alpha)| > 20 \text{ \AA}$ criterion are predominantly of lower mass, whereas the more massive objects have already ceased accretion and no longer meet this requirement. Obviously, many additional sources (both young and old) show weaker $H\alpha$ excess (orange points in Fig. 4), but, as discussed in Section 4, their nature is less certain because they may include objects dominated by chromospheric activity rather than accretion.

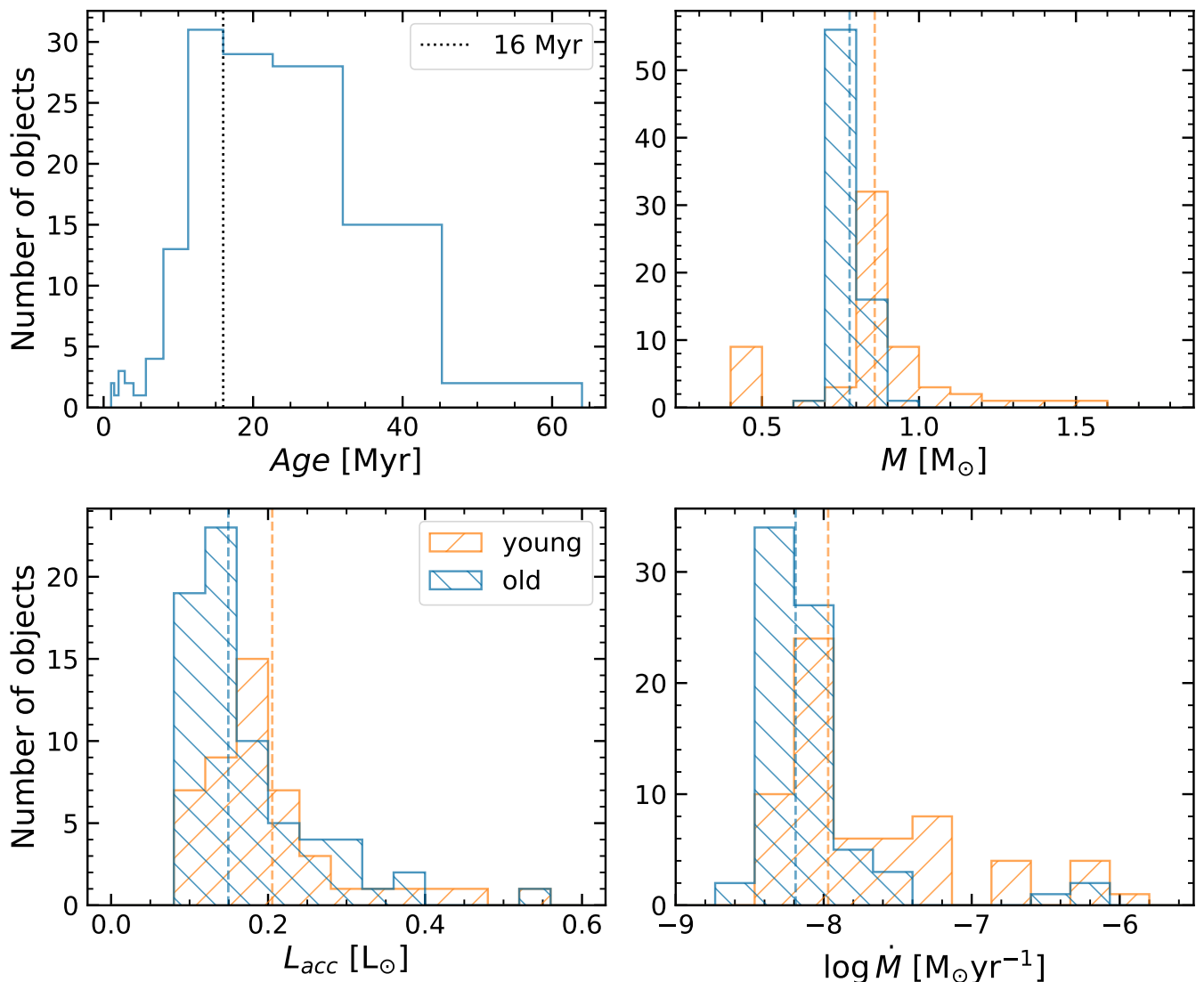


Fig. 6. Histograms showing the distribution of age (*top left*), mass (*top right*), accretion luminosity (*bottom left*), and mass accretion rate (*bottom right*) determined for the 137 bona fide PMS stars. The blue (orange) histograms represent the stars older (younger) than 16 Myr. Dashed vertical lines indicate the median of the respective distribution.

4.2. Accretion luminosity and mass accretion rate

The $H\alpha$ luminosity was computed from the observed line flux at the stellar surface as

$$L_{H\alpha} = 4\pi R^2 F_{H\alpha}, \quad (2)$$

using the standard definition of luminosity for a spherical emitter (see e.g. Mihalas 1978). In our specific case $F_{H\alpha}$ is the difference between the observed $H\alpha$ flux and the theoretical $H\alpha$ flux from the model atmospheres by Bessell et al. (1998). In turn, the observed $F_{H\alpha,obs}$ flux is obtained by multiplying the observed count rate in the $H\alpha$ band by the specific inverse sensitivity η and by the rectangular width RW of the F656N band, as per the equation

$$F_{H\alpha,obs} = 10^{-0.4(m_{H\alpha}-m_0)} \eta RW. \quad (3)$$

The inverse sensitivity η represents the flux that a source needs to have to produce a count rate of 1 e s^{-1} for a constant F_λ (Bohlin et al. 2020) and corresponds to $1.538 \times 10^{-17} \text{ erg cm}^{-2} \text{ s}^{-1} \text{ \AA}$ for

the specific $H\alpha$ filter of the HST/WFC3 camera. For the same instrumental set-up $RW = 17.68 \text{ \AA}$, while m_0 is the zero-point magnitude for $H\alpha$ (Table 2). The $H\alpha$ flux is then obtained by simply subtracting the theoretical flux ($F_{H\alpha,B}$) from the observed flux ($F_{H\alpha,obs}$):

$$F_{H\alpha} = F_{H\alpha,obs} - F_{H\alpha,B}. \quad (4)$$

The relationship between the accretion luminosity and the $H\alpha$ luminosity is unknown, but previous studies in this series (De Marchi et al. 2011a, 2013, 2017; Beccari et al. 2015; Biazzo et al. 2019; Carini et al. 2022; Tsilia et al. 2023; Vlasblom & De Marchi 2023) have followed the empirical relationship between $L_{H\alpha}$ and L_{acc} derived by De Marchi et al. (2010), based on the analysis of the observations of a number of T Tauri stars by Dahm (2008). That relationship is based on the assumption that L_{acc} and $L_{H\alpha}$ are linearly related (see e.g. Clarke & Pringle 2006), in a magnetospheric accretion scenario.

More recent studies by Alcalá et al. (2017) of a larger sample of T Tauri stars in Lupus revisited the matter and the authors

Table 4. Mass accretion rates for PMS stars inside NGC 346 proper and in the region studied here, per age group.

Age group	NGC 346 proper		NGC 346 periphery (this work)	
	Median \dot{M}_{acc}	No. of objects	Median \dot{M}_{acc}	No. of objects
Younger than 8 Myr	$(1.1 \pm 0.7) \times 10^{-7}$	345	$(6 \pm 4) \times 10^{-8}$	19
Between 8 and 20 Myr	$(5.0 \pm 2.0) \times 10^{-8}$	75	$(8 \pm 3) \times 10^{-9}$	59
Older than 20 Myr	$(1.5 \pm 0.6) \times 10^{-8}$	412	$(6 \pm 2) \times 10^{-9}$	59

Notes. For each age group, the median mass accretion rates and corresponding median absolute deviations (in units of $M_{\odot} \text{ yr}^{-1}$) are indicated, together with number of objects in that group.

concluded that a purely empirical fit to the data suggests a non-linear relationship. However, in the range of interest in this work, $0.1 \lesssim L(H\alpha) \lesssim 0.6$, the differences in L_{acc} implied by the two relationships is considerably smaller than the uncertainties intrinsic to the relationships themselves. Therefore, for the sake of comparison with previous works by our team, we continue to use the linear relationship of De Marchi et al. (2010) given by

$$\log L_{\text{acc}} = (1.72 \pm 0.25) + \log L_{H\alpha}. \quad (5)$$

We note that the observations in the $H\alpha$ band are not simultaneous with those in the continuum bands (obtained with both HST and *Gaia*). This can introduce an uncertainty on the derived $H\alpha$ luminosity. To estimate its impact, it is worth recalling that accretion-dominated T Tauri stars exhibit optical colour changes of typically $\Delta(V - I) \simeq 0.1 - 0.4$ mag, reaching $\simeq 0.5$ mag in strong accretors, and they become systematically bluer when brighter (Cody et al. 2014; Venuti et al. 2015; Stauffer et al. 2014). With reference to Fig. 4, this implies a difference of at most ~ 0.2 mag in the $V - H\alpha$ colour for the continuum under $H\alpha$, indicated by the dot-dashed line. Since our bona fide PMS candidates (orange dots in Fig. 4) have a median $\Delta(V - H\alpha) \simeq 1.2$ mag, the resulting uncertainty on $L(H\alpha)$ is about 20%. In fact, in most cases $L(H\alpha)$ will be brighter by that amount, since we are more likely to detect the $H\alpha$ excess during a burst, when $(V - I)$ is bluer.

The accretion luminosity derived with Eq. 5 can be converted to a mass accretion rate (\dot{M}_{acc}) through the free-fall equation

$$L_{\text{acc}} \simeq \frac{GM_* \dot{M}_{\text{acc}}}{R_*} \left(1 - \frac{R_*}{R_{\text{in}}}\right), \quad (6)$$

where G is the gravitational constant, M_* is the mass of the star, R_* its (photospheric) radius, and R_{in} the inner radius of the accretion disc. The value of R_{in} depends on factors such as the coupling of the accretion disc to the stellar magnetic field, which we cannot measure with our observations. Therefore, we adopted $R_{\text{in}} = 5R_*$ for each of the PMS stars, following Gullbring et al. (1998).

The resulting distribution of accretion luminosities and mass accretion rates can be found in the bottom panels of Fig. 6. There is no significant difference between the median accretion luminosity and mass accretion rate for the young and old PMS stars within the uncertainties, but old PMS objects tend to have lower accretion luminosities and mass accretion rates, as one would expect in general. A median mass accretion rate of $\dot{M} = (1.1 \pm 0.5) \times 10^{-8} M_{\odot} \text{ yr}^{-1}$ and $(6.5 \pm 1.7) \times 10^{-9} M_{\odot} \text{ yr}^{-1}$, with the uncertainties being the median absolute deviation, are found for the young and old group, respectively. These values are lower than those found with the same method for the main star forming cluster NGC 346 (De Marchi et al. 2011a), and recently confirmed spectroscopically by De Marchi et al. (2024),

although in our sample there are a number of young PMS objects with comparable mass accretion rates between 10^{-8} and $10^{-7} M_{\odot} \text{ yr}^{-1}$.

To further investigate the difference in \dot{M}_{acc} between the outer field studied here and NGC 346 proper (see Fig. 2), we took the \dot{M}_{acc} values of all PMS stars in the main cluster from De Marchi et al. (2011a) and divided both that sample and our PMS sample into three age groups. The ages were chosen so that the sample in our outer-field is split into roughly equal-number subsets, namely objects younger than 8 Myr, older than 20 Myr, and those in between. The median mass accretion rates of the three groups and their uncertainties are shown in Table 4. Clearly, \dot{M}_{acc} is consistently lower for stars of the same age and mass in the outer field studied here than in the central NGC 346 cluster, as has already been observed for other lower density star-forming regions in the Magellanic Clouds (see e.g. Biazzo et al. 2019; Carini et al. 2022; Vlasblom & De Marchi 2023; Tsilia et al. 2023).

5. Effect of nearby massive stars

Given the proximity of the studied region to the NGC 346 cluster itself, it is interesting to investigate whether there is a relationship between the location and physical properties of the PMS stars in this field and the massive stars in NGC 346. The relative distribution is shown in Fig. 7 and we used it to look for any gradient in the direction of the cluster. As for the spatial distribution of the PMS stars, these objects are distributed rather uniformly across the field and we do not observe more active star formation in the direction of NGC 346, nor does the $L(H\alpha)$ luminosity of the PMS stars appear to correlate with their projected distance from NGC 346. This is not surprising, considering that the projected distance to the centre of NGC 346 is about 164 pc.

However, the data reveal an interesting trend between the $L(H\alpha)$ luminosity of the PMS stars and their distance from the barycentre of a small group of massive stars in the west-southwest portion of the field, whose ionising radiation might be contributing to the dissipation of the circumstellar discs through photoevaporation (Ramírez-Tannus et al. 2025). Following De Marchi et al. (2010), we selected young massive stars with $\log(T_{\text{eff}}/\text{K}) \geq 4.4$ and $\log(L/L_{\odot}) \geq 4$, having adopted a distance of 62.5 kpc (Graczyk et al. 2020) and $A_V = 0.84$ (see Section 3). We note that the values of T_{eff} were derived from the $V - I$ colours, using the model atmospheres of Bessell et al. (1998), and as such they might underestimate the actual effective temperatures. The 17 objects selected in this way, with $25,000 \text{ K} \lesssim T \lesssim 32,000 \text{ K}$, correspond to sources in the upper part of the MS with $V < 17.5$ mag and $V - I < 0.12$ mag. Their positions are shown by orange star symbols in Fig. 7. Stars with a redder $V - I$ colour are not considered here, since we are interested in the effect of strong ultraviolet radiation originating from these massive objects. In total, 12 of these sources fall within the

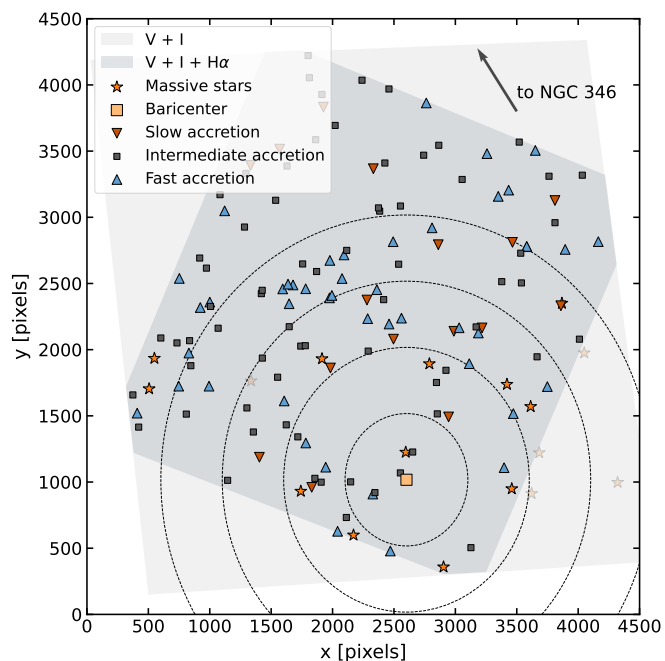


Fig. 7. Distribution of PMS stars in the field, colour-coded by their relative mass accretion rate: in blue ‘fast’ accretors ($\dot{M}_{\text{acc}} > 10^{-8} M_{\odot} \text{yr}^{-1}$), in dark grey ‘intermediate’ accretors ($10^{-8.3} M_{\odot} \text{yr}^{-1} < \dot{M}_{\text{acc}} < 10^{-8} M_{\odot} \text{yr}^{-1}$), and in red ‘slow’ accretors ($\dot{M}_{\text{acc}} < 10^{-8.3} M_{\odot} \text{yr}^{-1}$). The most massive young (non-PMS) stars are plotted in orange, with their barycentre in yellow. Radial shells around this barycentre are shown, as well as the outlines of the imaged fields (see Fig. 2) and an arrow pointing towards the centre of the NGC 346 cluster proper.

field of the $H\alpha$ observations and have reliable $H\alpha$ photometry. Using the 10 Myr isochrone in Fig. 3, we derived approximate masses for these objects, all of which are larger than $\sim 10.5 M_{\odot}$. We also used the 10 Myr isochrone to assign masses to stars in the range $17.5 \text{ mag} < V < 18.5 \text{ mag}$ and with $V - I < 0.08 \text{ mag}$, which we used to compute the mass function (see below). Since these sources have $T_{\text{eff}} < 25,000 \text{ K}$, their ionising photon rate would not contribute significantly to the photoevaporation of the discs.

The yellow square in Fig. 7 corresponds to the barycentre of the ionising photon rates of the 17 massive stars, taken for each source from Panagia (1973) and computed under the simplifying assumption that all objects are at the same distance from us on the plane of the sky. We note that all of the most massive stars are concentrated in the lower (southern) part of the image, suggesting a recent star formation episode in that part of the region.

From the barycentre, we moved radially outwards, dividing the region into concentric circular annuli (‘shells’) and considered the stars in each consecutive shell, as indicated by dashed circular lines in Fig. 7. The radial width of the shells is $15''$, corresponding to a projected distance of roughly 4.4 pc. The total number of bona fide PMS stars inside each shell was counted, as well as the fraction of the total number of stars that they represent. These fractions are shown in Fig. 8 (left). In addition, the average mass accretion rate of the stars in each shell was computed, as shown in the same figure on the right. The uncertainties shown in the figure represent the standard deviation within the shells. As mentioned above, this is a simplifying two-dimensional projection, because the distance to each individual star is not known. However, we are considering an ordinary region of the SMC field, which is known to be dominated by old

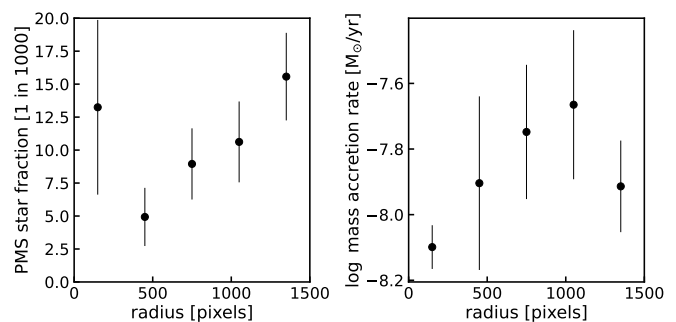


Fig. 8. Left: Fraction of PMS stars relative to the total number of stars. Right: \dot{M}_{acc} of the PMS stars averaged over each shell.

and intermediate-age stars (see e.g. Hodge 1985; Harris & Zaritsky 2004), so there is no reason to expect large anisotropies.

Indeed, the non-PMS stars in this field are distributed evenly in number across the region, so if also the PMS stars had a uniform distribution then one would expect the ratio of PMS and non-PMS stars to remain constant across the field. This would correspond to a horizontal trend in Fig. 8. Similarly, if there were no influence due to the environment, the average \dot{M}_{acc} would remain constant across each shell. Instead, what is observed is a general increase in both the PMS star fraction and the mass accretion rate when moving radially away from the barycentre of the young massive stars. The uncertainties are largest in the central bin, where only six PMS stars are present, and the resulting fraction is affected by small-number statistics. (We note that the trends are still evident if the size of the shells is reduced to $10''$, albeit with a larger scatter.)

The observed trends suggest that there might be an interaction between this young population of massive stars and the PMS stars. In particular, the radiation of the nearby massive stars might be eroding the discs, possibly through both ionisation and photoevaporation (see e.g. Störzer & Hollenbach 1999; Adams et al. 2004), thereby reducing disc lifetimes and causing the accretion process to fade.

Of course, these trends must be interpreted with caution, since neither the PMS stars nor the massive stars responsible for the ionising radiation have known positions along the line of sight. The massive stars themselves are spatially scattered, and the lack of three-dimensional information introduces additional uncertainty in the location of their barycentre. For this reason, while the data indicate the presence of an environmental effect possibly caused by the massive stars, the available information does not allow a fully quantitative characterisation of its strength.

To investigate the nature of these massive objects, it is useful to understand whether they formed in situ in their current location or are instead in some way related to NGC 346. This helps in clarifying the role that NGC 346 may have played in shaping the stellar populations observed in the surrounding region. To this end, we considered the kinematics of the field. Using proper motions from the *Gaia* DR3 catalogue (Gaia Collaboration et al. 2023) for the young massive stars, we find that the bulk motion is dominated by the proper motion of the SMC itself. In our sample, the median proper motions components towards the west and north as measured by *Gaia* are, respectively, $\mu_W = -0.75 \text{ mas yr}^{-1}$ and $\mu_N = -1.27 \text{ mas yr}^{-1}$ (with sample standard deviations of $\sigma_{\mu_W} = 0.21 \text{ mas yr}^{-1}$ and $\sigma_{\mu_N} = 0.12 \text{ mas yr}^{-1}$), compared to the systemic proper motion components of the SMC of $\mu_W = -0.82 \text{ mas yr}^{-1}$ and $\mu_N = -1.21 \text{ mas yr}^{-1}$. After sub-

tracting the systemic components, there remains no preferential direction of motion, nor evidence of rotation, for any of the massive stars in our field. This suggests that the young massive stars have likely formed there, and there is no detectable effect of outflow or rotation due to the massive nearby NGC 346 cluster.

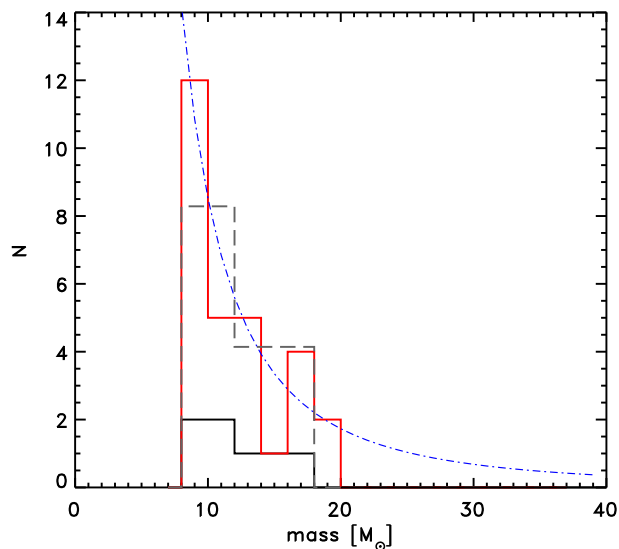


Fig. 9. Histograms of the number of massive stars ($8 - 20 M_{\odot}$) in our region (red line) and in the ONC (black line). The dashed line represents the IMF of the ONC rescaled to match the number of objects under the red line. The best fitting standard Kroupa (2002) IMF is shown by the dot-dashed line.

The area that we surveyed represents a good example of massive star formation in the field. It is known that a non-negligible fraction of massive stars in the Magellanic Clouds are found outside prominent clusters: while many are runaways (see e.g. Evans et al. 2011), about 35% are consistent with in situ formation in sparse groups or isolation (Oey et al. 2004, 2013). To characterise the population of massive stars in this region, we computed the mass function using the masses estimated through comparison with the 10 Myr isochrone (see above). The distribution of stars with masses of $8 - 20 M_{\odot}$ (red histogram in Fig. 9) agrees well with the Kroupa (2002) initial mass function (IMF; dot-dashed line). For comparison, we also consider the IMF of the Orion Nebula Cluster (ONC; Hillenbrand 1997; Da Rio et al. 2010) over the same mass range (black solid line), together with a version rescaled by a factor of 4.1 (dashed line) to match the number of objects observed in our region in the $8 - 20 M_{\odot}$ interval. The comparison is necessarily approximate because we derived the masses of our stars from their photometry and cannot assess their multiplicity, which is expected to be high for massive objects in general and even more so at low metallicities (Sana et al. 2012; Shenar et al. 2024). The ONC currently hosts an even more massive object, the $34 M_{\odot}$ θ^1 Ori C1 (Kraus et al. 2007), which is not included in the IMF of Fig. 9 because in a field like ours, with an age of 10 Myr and older, objects of that mass are expected to have already exploded as Type II supernovae and would no longer contribute to the mass function.

The surface density of massive stars in our field is considerably lower than in a typical stellar cluster: the $8 - 20 M_{\odot}$ stars are distributed over an area of ~ 12 pc radius, whereas in the ONC they are contained within ~ 0.6 pc. However, despite the lower surface density, the massive stars that we detect are more than four times those in the ONC in the same range. This compari-

son serves to highlight the potentially significant contribution of field star formation to the overall mass budget of galaxies.

6. Comparison with JWST observations

JWST/NIRCam observations exist in a field partly overlapping with the one studied in this work (Fig. 2; see Section 2). Because the NIRCam observations cover near-IR wavelengths ($0.9 - 4.3 \mu\text{m}$), they are complementary in wavelength to our HST data, which probe the optical regime including $H\alpha$; together they allow us to detect both accretion signatures and circumstellar-disc emission from the same stars. In this work we used the photometric analysis of the NIRCam data provided by K. Fahrion (private comm.), following the workflow discussed in Fahrion & De Marchi (2024), to identify and measure the magnitudes of the sources in the field observed with NIRCam around NGC 346 (see Fig. 1). We constructed a CMD in the F090W and F227W bands for the overlapping area, which is shown in the left panel of Fig. 10. The right panel reproduces the HST CMD from Fig. 3 for the same region.

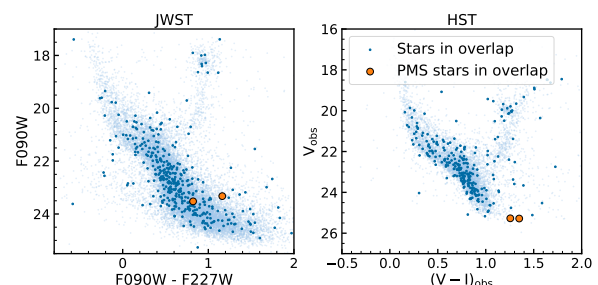


Fig. 10. CMDs obtained with the JWST/NIRCam (*left*) and HST (*right*) photometry. In the left panel, light blue dots are JWST sources outside the HST–JWST overlapping region, and blue dots are sources only included in the field observed with JWST. In the right panel, blue marks the HST sources in the overlapping region. The orange points indicate the two bona fide PMS stars with reliable NIRCam photometry; they are shown in both panels.

Of the 137 bona fide PMS stars, four fall within the field covered by NIRCam. Two of these lie too close to the detector edges and as such lack reliable photometry, leaving two well-measured PMS candidates for comparison. Their identification numbers are 12510 and 12635 in Table 2. One of the two PMS stars ends up with a significantly redder F090W–F227W colour than the bulk of MS stars, further strengthening the notion that this object is indeed a PMS star surrounded by a dusty circumstellar disc that causes some near-IR excess. Additionally, the other star, with a F090W–F227W colour of 0.8, is consistent with the CMD position of PMS stars on the central NGC 346 cluster as observed by Habel et al. (2024) with NIRCam.

The JWST photometry is complementary to the HST photometry and reveals different properties of the stars. While $H\alpha$ excess indicates accretion from the circumstellar disc onto the star, near-IR excess originates from thermal disc emission (see e.g. Cusano et al. 2011). Detecting both would be a strong sign of the PMS nature, although the absence of significant near-IR excess cannot rule out the PMS nature of the objects, particularly for old PMS stars with evolved and transitional discs with inner dust cavities (see e.g. Sicilia-Aguilar et al. 2010). Similarly lack of $H\alpha$ excess emission at the 5σ level of more does not imply that the star is not accreting, rather that accretion might be too weak to be detected with our method.

Table 5. NIRCam photometric band parameters.

Band	m_0	η_{MJSR}	BW_{eff}
F090W	26.13	3.282	0.194
F115W	25.95	2.698	0.225
F182M	25.01	3.328	0.238
F187N	22.26	38.93	0.024
F277W	25.09	0.491	0.672
F356W	24.72	0.408	0.787
F405N	20.89	9.711	0.046
F430M	22.67	1.880	0.228

Notes. For each filter, the table provides the zero-point magnitude (m_0), the conversion factor from count s^{-1} to MJy sr^{-1} (η_{MJSR}), and the effective bandwidth (BW_{eff}).

Using all available JWST bands listed in Table 5, we constructed a spectral energy distribution (SED) for the two PMS stars in the overlapping region (Fig. 11). The SED traces the flux density as a function of wavelength and directly probes any near-IR excess above the stellar photosphere. We converted the magnitudes to flux density using

$$f_{\nu} = 10^{-0.4(m-m_0)} \eta_{\text{MJSR}} BW_{\text{eff}}, \quad (7)$$

where m is the measured magnitude, m_0 the zero-point (Vega) magnitude, η_{MJSR} the conversion factor ('PHOTMJSR') from counts per second to MJy sr^{-1} , and BW_{eff} the effective bandwidth of the respective filter. η_{MJSR} is taken from the header of the .fits files. We took the literature values from the JWST documentation for the zero-point magnitudes (Rigby et al. 2023; Gordon et al. 2022) and effective bandwidths (Rieke et al. 2008; Tokunaga & Vacca 2005). We note that the overlapping region falls entirely within the B1 detector on NIRCam; we thus adopted the values specifically for B1 (or B). They can be found in Table 5.

Shown in Fig. 11 are the SEDs for the two PMS stars in the overlapping region. These are compared to the model atmosphere of a MS 6500 K star, again by Bessell et al. (1998). For the sake of comparison, the SEDs are normalised to this model continuum at 9000 Å, the lowest central wavelength in the JWST photometry. Compared to the model atmosphere for MS stars, the two PMS stars exhibit a moderate near-IR excess at all wavelengths. The observed excess is fully consistent with the one measured spectroscopically for PMS stars in the core of NGC 346 by De Marchi et al. (2024). We note that the data point at ~ 18700 Å captures the flux density measured through the F187N narrow-band filter of NIRCam and includes not only the stellar continuum but also the Pa α emission line, which is the strongest H recombination line in this wavelength range and is connected with the accretion process. However, even if that data point is neglected, the SED of the stars is still consistent with the presence of a dusty disc.

The detection of both H α excess (from our HST photometry) and near-IR excess (from JWST) for these two objects constitutes strong evidence for their PMS nature. Spectroscopic follow-up would allow a direct measurement of line strengths and profiles, to unambiguously confirm accretion activity and better constrain the disc structure.

7. Summary and conclusions

In this work, we studied the star formation in a field outside the cluster NGC 346 in the SMC by analysing HST photometry in

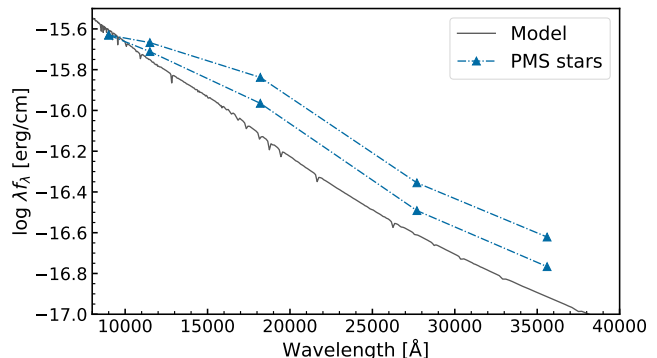


Fig. 11. Model SED showing the logarithm of the flux density as a function of wavelength, zoomed in on the IR tail. Shown in blue are the two overlapping PMS stars and their flux density at different wavelengths. All curves are anchored to the model at 9000 Å

the V, I, and H α bands. A total of 12 649 sources were selected as having reliable photometry with uncertainties $\sigma_{\text{H}\alpha} \leq 0.3$ mag and $\sigma_{\text{VI}} \leq 0.1$ mag. We found a population of PMS stars and analysed their distribution and physical properties, studying the effect of young massive stars on the PMS population, as well as the proper motion of the stars in this region. Finally, we compared our results with JWST photometric observations of an overlapping region. The main results of this work can be summarised as follows:

1. The CMD shows evidence of populations of roughly 10, 60, 400 Myr, and 5 Gyr, which agrees with known star-forming episodes in the SMC.
2. We identified 137 bona fide PMS stars with H α excess greater than 5σ and $|W_{\text{eq}}| \geq 20$ Å in emission. The detected H α emission suggests the presence of an accreting PMS population in this low-density field, well outside the boundaries of the main NGC 346 cluster.
3. Most PMS stars are around 16 Myr old, with $\langle M \rangle = 0.80 \pm 0.16 M_{\odot}$.
4. Dividing the PMS stars into two groups younger and older than 16 Myr, we find that the younger stars have a higher average mass, accretion luminosity, and mass accretion rate, as expected.
5. The PMS stars in the studied region have an overall median mass accretion rate of $\dot{M}_{\text{acc}} = (8 \pm 3) \times 10^{-9} M_{\odot} \text{ yr}^{-1}$. This is comparable to other low-density star-forming regions in the SMC (Vlasblom & De Marchi 2023; Tsilia et al. 2023), but lower than in the NGC 346 cluster, where median values range from $(1.5 \pm 0.6) \times 10^{-8}$ to $(1.1 \pm 0.7) \times 10^{-7} M_{\odot} \text{ yr}^{-1}$ depending on the age group (De Marchi et al. 2011a).
6. The PMS stars are distributed uniformly across the field without a significant spatial gradient; a local under-density is found in the southern portion of the field, coinciding with the concentration of massive stars.
7. The fraction of PMS stars relative to the total stellar population decreases closer to the barycentre of the young massive stars, and so does the mass accretion rate. This suggests an interaction between the PMS stars and the group of massive stars, which might accelerate disc dispersal.
8. The massive stars, in the range 8 – 20 M_{\odot} , are four times more numerous than those in the ONC, and their number distribution agrees well with a standard Kroupa IMF.
9. The *Gaia* DR3 proper motions of the massive stars are consistent with the bulk motion of the SMC, with no residual

preferential direction, indicating that neither outflow nor rotation due to the nearby NGC 346 cluster is detectable.

10. Comparing HST to JWST photometry in the overlapping region, we find that two bona fide PMS stars show near-IR and Pa α excess, consistent with the presence of dusty circumstellar discs.

With this work, we have extended the knowledge of star formation in a seemingly inconspicuous region in the SMC, well outside the high-density active NGC 346 star-forming region, where metallicities are comparable to those prevailing in the early Universe. The physical properties of the population of PMS stars that we find appear to be affected by the ionising radiation of the coeval nearby massive stars. These results highlight the contribution of low-density field environments to the overall star formation budget, and the role that local massive stars play in shaping accretion processes in their vicinity. Rather than being confined to dense clusters, massive stars in the field appear capable of shaping their surroundings, by contributing meaningfully to galactic evolution and influencing local star formation. As such, understanding the conditions that permit massive stars to form in isolation or sparse groups is essential for constructing more comprehensive models of stellar populations and determining their impact across different galactic contexts.

Data availability

Table 3 is only available in electronic form at the CDS via anonymous ftp to cdsarc.u-strasbg.fr (130.79.128.5) or via <http://cdsweb.u-strasbg.fr/cgi-bin/qcat?J/A+A/>.

Acknowledgements. We thank an anonymous referee for a careful reading of the manuscript and for constructive comments that helped us improve its clarity. We are grateful to Katja Fahrion for sharing with us her JWST/NIRCam photometry ahead of publication. This research is based on observations made with the NASA/ESA *Hubble* Space Telescope obtained from the Space Telescope Science Institute, which is operated by the Association of Universities for Research in Astronomy, Inc., under NASA contract NAS 5–26555. These observations are associated with programmes 10248 and 13009. This research has made use of Python, <https://www.python.org>, of NumPy (Harris et al. 2020), Astropy (Astropy Collaboration et al. 2013), and Matplotlib (Hunter 2007). This work has made use of data from the European Space Agency (ESA) mission *Gaia* (<https://www.cosmos.esa.int/gaia>), processed by the *Gaia* Data Processing and Analysis Consortium (DPAC, <https://www.cosmos.esa.int/web/gaia/dpac/consortium>). Funding for the DPAC has been provided by national institutions, in particular the institutions participating in the *Gaia* Multilateral Agreement. This work is based in part on observations made with the NASA/ESA/CSA *James Webb* Space Telescope and associated with programme 1227.

References

- Adams, F. C., Hollenbach, D., Laughlin, G., & Gorti, U. 2004, *ApJ*, 611, 360
 Alcalá, J. M., Manara, C. F., Natta, A., et al. 2017, *A&A*, 600, A20
 Astropy Collaboration, Robitaille, T. P., Tollerud, E. J., et al. 2013, *A&A*, 558, A33
 Baraffe, I., Chabrier, G., Allard, F., & Hauschildt, P. H. 2002, *A&A*, 382, 563
 Beccari, G., De Marchi, G., Panagia, N., et al. 2015, *A&A*, 574, A44
 Bell, C. P. M., Naylor, T., Mayne, N. J., Jeffries, R. D., & Littlefair, S. P. 2013, *MNRAS*, 434, 806
 Bessell, M. S., Castelli, F., & Plez, B. 1998, *A&A*, 333, 231
 Biazzo, K., Beccari, G., De Marchi, G., & Panagia, N. 2019, *ApJ*, 875, 51
 Bohlin, R. C. 2016, *AJ*, 152, 60
 Bohlin, R. C., Ryon, J. E., & Anderson, J. 2020, Instrument Science Report ACS 2020-8
 Bressan, A., Marigo, P., Girardi, L., et al. 2012, *MNRAS*, 427, 127
 Bromm, V. 2013, *Reports on Progress in Physics*, 76, 112901
 Carini, R., Biazzo, K., De Marchi, G., et al. 2022, *A&A*, 663, A74
 Chen, Y., Girardi, L., Fu, X., et al. 2019, *A&A*, 632, A105
 Clarke, C. J. & Pringle, J. E. 2006, *MNRAS*, 370, L10
 Cody, A. M., Stauffer, J., Baglin, A., et al. 2014, *AJ*, 147, 82
 Cox, A. N., ed. 2000, *Allen's Astrophysical Quantities*, 4th edn. (New York: Springer)
 Crutcher, R. M. 1999, *ApJ*, 520, 706
 Cusano, F., Ripepi, V., Alcalá, J. M., et al. 2011, *MNRAS*, 410, 227
 Da Rio, N., Robberto, M., Soderblom, D. R., et al. 2010, *ApJ*, 722, 1092
 Dahm, S. E. 2008, *AJ*, 136, 521
 De Marchi, G., Beccari, G., & Panagia, N. 2013, *ApJ*, 775, 68
 De Marchi, G., Giardino, G., Biazzo, K., et al. 2024, *ApJ*, 977, 214
 De Marchi, G. & Panagia, N. 2014, *MNRAS*, 445, 93
 De Marchi, G., Panagia, N., & Beccari, G. 2017, *ApJ*, 846, 110
 De Marchi, G., Panagia, N., & Romaniello, M. 2010, *ApJ*, 715, 1
 De Marchi, G., Panagia, N., Romaniello, M., et al. 2011a, *ApJ*, 740, 11
 De Marchi, G., Paresce, F., Panagia, N., et al. 2011b, *ApJ*, 739, 27
 Evans, C. J., Taylor, W. D., Hénault-Brunet, V., et al. 2011, *A&A*, 530, A108
 Fahrion, K. & De Marchi, G. 2024, *A&A*, 681, A20
 Gaia Collaboration, Vallenari, A., Brown, A. G. A., et al. 2023, *A&A*, 674, A1
 Girardi, L., Dalcanton, J., Williams, B., et al. 2008, *PASP*, 120, 583
 Gordon, K. D., Bohlin, R., Sloan, G. C., et al. 2022, *AJ*, 163, 267
 Graczyk, D., Pietrzyński, G., Thompson, I. B., et al. 2020, *ApJ*, 904, 13
 Gullbring, E., Hartmann, L., Briceño, C., & Calvet, N. 1998, *ApJ*, 492, 323
 Habel, N., Nally, C., Lenkić, L., et al. 2024, *ApJ*, 971, 108
 Haid, S., Walch, S., Seifried, D., et al. 2018, *MNRAS*, 478, 4799
 Harris, C. R., Millman, K. J., van der Walt, S. J., et al. 2020, *Nature*, 585, 357
 Harris, J. & Zaritsky, D. 2004, *AJ*, 127, 1531
 Hennekemper, E., Gouliermis, D. A., Henning, T., Brandner, W., & Dolphin, A. E. 2008, *ApJ*, 672, 914
 Hillenbrand, L. A. 1997, *AJ*, 113, 1733
 Hillenbrand, L. A. & White, R. J. 2004, *ApJ*, 604, 741
 Hodge, P. 1985, *PASP*, 97, 530
 Hunter, J. D. 2007, *Computing in Science and Engineering*, 9, 90
 Jeffries, R. D., Jackson, R. J., Franciosini, E., et al. 2017, *MNRAS*, 464, 1456
 Jones, O. C., Nally, C., Habel, N., et al. 2023, *Nature Astronomy*, 7, 694
 Kalirai, J. S., MacKenty, J., Bohlin, R., et al. 2009, Instrument Science Report WFC3 2009-30
 Kraus, S., Balega, Y. Y., Berger, J.-P., et al. 2007, *A&A*, 466, 649
 Kroupa, P. 2002, *Science*, 295, 82
 Krumholz, M. R. 2012, *ApJ*, 759, 9
 Krumholz, M. R., Klein, R. I., & McKee, C. F. 2012, *ApJ*, 754, 71
 Madden, S. C., Rémy-Ruyer, A., Galametz, M., et al. 2013, *PASP*, 125, 600
 McKee, C. F. & Ostriker, E. C. 2007, *ARA&A*, 45, 565
 McSwain, M. V. & Gies, D. R. 2005, *ApJ*, 622, 1052
 Mihalas, D. 1978, *Stellar Atmospheres*, 2nd edn. (San Francisco: W. H. Freeman)
 Nota, A., Sirianni, M., Sabbi, E., et al. 2006, *ApJ*, 640, L29
 Nozaki, S. & Machida, M. N. 2023, *MNRAS*, 519, 5017
 Oey, M. S., King, N. L., & Parker, J. W. 2004, *AJ*, 127, 1632
 Oey, M. S., Lamb, J. B., Kushner, C. T., Pellegrini, E. W., & Graus, A. S. 2013, *ApJ*, 768, 66
 Panagia, N. 1973, *AJ*, 78, 929
 Pastorelli, G., Marigo, P., Girardi, L., et al. 2019, *MNRAS*, 485, 5666
 Ramírez-Tannus, M. C., Bik, A., Getman, K. V., et al. 2025, *A&A*, 701, A139
 Rémy-Ruyer, A., Madden, S. C., Galliano, F., et al. 2014, *A&A*, 563, A31
 Rieke, G. H., Blaylock, M., Decin, L., et al. 2008, *AJ*, 135, 2245
 Rigby, J., Perrin, M., McElwain, M., & Kimble, R. 2023, *PASP*, 135, 048001
 Rolleston, W. R. J., Dufton, P. L., McErlean, N. D., & Venn, K. A. 1999, *A&A*, 348, 728
 Romaniello, M. 1998, PhD thesis, Scuola Normale Superiore, Pisa, Italy
 Russell, S. C. & Dopita, M. A. 1992, *ApJ*, 384, 508
 Sabbi, E., Sirianni, M., Nota, A., et al. 2007, *AJ*, 133, 44
 Sana, H., de Mink, S. E., de Koter, A., et al. 2012, *Science*, 337, 444
 Shenar, T., Bodensteiner, J., Sana, H., et al. 2024, *A&A*, 690, A289
 Shu, F. H., Adams, F. C., & Lizano, S. 1987, *ARA&A*, 25, 23
 Sicilia-Aguilar, A., Henning, T., & Hartmann, L. W. 2010, *ApJ*, 710, 597
 Stauffer, J., Cody, A. M., Baglin, A., et al. 2014, *AJ*, 147, 83
 Störzer, H. & Hollenbach, D. 1999, *ApJ*, 515, 669
 Tang, J., Bressan, A., Rosenfield, P., et al. 2014, *MNRAS*, 445, 4287
 Tognelli, E., Prada Moroni, P. G., & Degl'Innocenti, S. 2011, *A&A*, 533, A109
 Tokunaga, A. T. & Vacca, W. D. 2005, *PASP*, 117, 421
 Tsilia, S., De Marchi, G., & Panagia, N. 2023, *A&A*, 675, A203
 Venuti, L., Bouvier, J., Irwin, J., et al. 2015, *A&A*, 581, A66
 Vlasblom, M. & De Marchi, G. 2023, *A&A*, 675, A204
 White, R. J. & Basri, G. 2003, *ApJ*, 582, 1109